AEROTHERMODYNAMIC FIELD PAST A REENTRY CAPSULE FOR SAMPLE RETURN MISSIONS

Antonio Viviani*, Giuseppe Pezzella, Carmine Golia***
***Seconda Università di Napoli (SUN), via Roma 29, 81031 Aversa, Italy.**
**** Centro Italiano Ricerche Aerospaziali (CIRA), via Maiorise, 81043 Capua, Italy.**
antonio.viviani@unina2.it; g.pezzella@cira.it; carmine.golia@unina2.it.

Keywords: *Aerodynamics, Aerothermodynamics, Super-orbital Re-entry, Hypersonic non-equilibrium flow, Computational Fluid Dynamics*

Abstract

This paper deals with the computational fluid dynamics analysis of a capsule entering the Earth atmosphere, with the aim of supporting sample return system design studies.

Several fully three-dimensional Computational Fluid Dynamics analyses, for non-equilibrium reacting gas approximations, have been performed to assess the flowfield environment past a sphere-cone capsule. Hence, the aerodynamic and aerothermodynamic performance of the entry vehicle in the framework of a super-orbital re-entry scenario is addressed.

1 Capsule for Sample Return Missions

An important step forward for Space Exploration activities and for a more accurate knowledge of the Earth, and Universe is to develop the capability to send vehicles into space which select, collect and finally return samples from other celestial bodies to Earth where to perform their analysis.

To return these samples to Earth, however, very high-speed re-entry trajectories must be performed. Therefore, the design of a re-entry sample return vehicle (SRV) requires strong technological bases and relies on a good understanding of the loading environment encountered during the super-orbital re-entry.

A high speed Earth entry vehicle has the following characteristics: entry velocity higher or equal to 11.7 km/s (compared to 7.5 km/s for the US Space Shuttle); very high heat fluxes (more than 10 MW/m^2) and heat loads (in the range of 500 MJ/m^2), where the radiative part is important.

In this framework a capsule configuration has been selected and a re-entry trajectory has been computed to address the sample return vehicle design.

1.1 Capsule Configuration

The selected shape is a sphere-cone aeroshell with a 45 deg half cone angle, a 1.1 m diameter front shield and a smaller back-cover that is shown in Fig. 1.

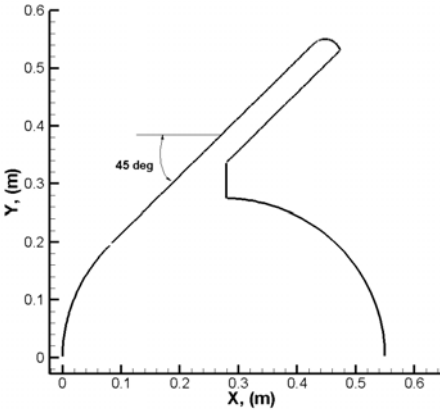

Fig. 1 Capsule geometry with quotes.

The layout and design of the capsule assure a safe return of the sample canister, relying on a fully passive concept [1].

The selection of such a kind of aeroshell was the result of a trade-off design among hypersonic drag (aeroheating), subsonic drag (impact velocity) and subsonic stability (available crush stroke) [1]. The SRV nose radius is equal to 0.275 m; while at the shoulder

the radius of curvature is equal to about 0.0275 m. The capsule vehicle, including margins, is estimated to weigh about 50 kg. The CoG is foreseen at 26.5% from the nose relatively to the SRV diameter. This value is almost compliant with the stability requirements of such a shape, as clarified hereinafter.

2 Re-entry Flight Scenario

The flight design scenario of the SRV concept is shown in Fig. 2. It refers to an Earth steep descent (i.e., -12.5 deg of flight path angle).

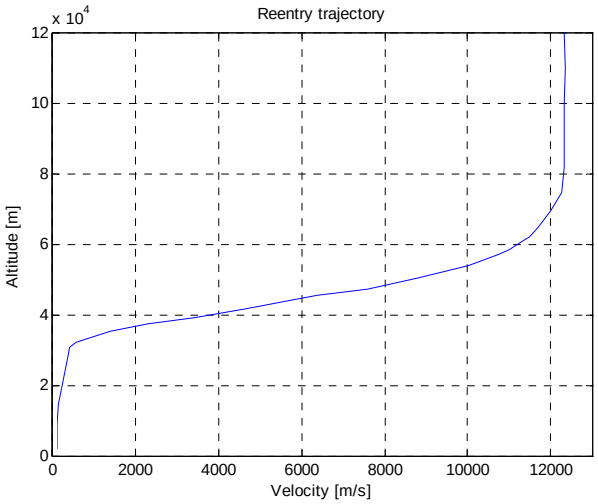

Fig. 2 Altitude evolution vs. velocity.

Such a trajectory allows predicting the flow field around the proposed capsule because of it provides freestream conditions for CFD computations. It also defines the aerothermodynamic environment the capsule has to withstand during descent. For instance, the evolutions of heat fluxes (convective and radiative part) are presented in Fig. 3. In the preliminary design the convective and radiative heat fluxes have been estimated by using analytical engineering correlations such as Scott relationship for convective heat flux and Tauber-Sutton one for the radiative heat flux estimation [2][3]. All the estimations provided in Fig. 3 are extremely important for designing the capsule heat shield. Indeed, the aeroheating environment dictates, in fact, the type and size of the thermal protection system (TPS) to use.

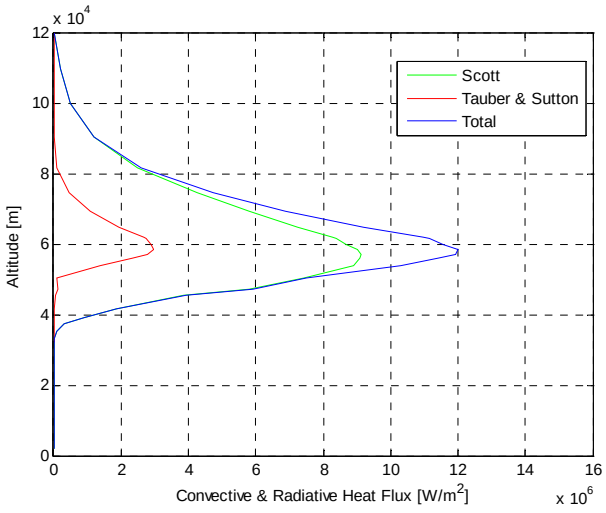

Fig. 3 Heat Flux vs. altitude.

Peak heat rate generally determines the range of possible thermal protection material (TPM) while the integrated heat load determines the thickness and hence the mass of the heat shield.

3 Design Approach and Used Tools

The SRV concept, during the re-entry at super-orbital speed, has a number of extreme loading flight conditions for which design analyses are required. It must return from outer space, fly trimmed throughout hypersonic and supersonic regimes until touchdown. Therefore, it is extremely important to understand the aerodynamics of the aircraft regardless of the flight regime. This is particularly the case for sample return missions where strong flowfield radiation and heatshield ablation may affect vehicle aerothermodynamic performances.

Indeed, due to the very high temperatures reached in the shock layer caused by the strong bow shock in front of the capsule, the gas not only dissociates and ionized but can also emit radiated energy which travels across the entire flowfield interacting with the gas itself. At the entry velocity foreseen for the capsule, this contribution, that is generally very low with respect to other “energies” in the flowfield, cannot be neglecting because it can cause an additional source of heat load at the wall to be taken into account [7]. From a general point of view, the flowfield and the radiative field are

coupled: the radiated energy travels across the flowfield, interacts with the fluid dynamic field which changes its configuration and causes the change of the radiated energy, and so on. From a mathematical point of view, this interaction is represented by a source term in the classical Navier-Stoke equation for the energy conservation which represents the quantity of radiated energy travelling across the flowfield.

In the present case, however, we consider a simplified, non-coupled, approach: it assumes that the energy emitted mainly just behind the shock region, travels towards the wall, being in part absorbed by the gas in the shock layer, without changing its structure and arrives at the wall increasing the total heat flux. Different results presented in literature provided that this uncoupled approach is conservative if applied to the radiative heat flux estimation at the wall [7].

In this work, the aerodynamic coefficients have been provided for different flight conditions along with the sizing flight trajectory, according to the trajectory-based design approach. The heat flux distributions, both convective and radiative one, are also provided for each trajectory design point.

In particular, the appraisal of the vehicle aerodynamic database (AEDB) was performed by means of both engineering-based tools and CFD computations; while the SRV aerothermodynamic database (ATDB) was accomplished by means Navier-Stokes CFD computations in thermo-chemical non-equilibrium conditions. Then results of those CFD simulations are provided to PARADE code for the estimation of the radiative heat fluxes coming from the plasma flow in the shock layer [4].

The range between Mach 3 and 41.54 was analyzed. In the present analysis only continuum regime (supersonic and hypersonic speed ranges) with the air modeled as a mixture of several gases (including also those coming from the heat shield ablation) has been studied.

3.1 Engineering-based tool

Engineering based aerodynamic analyses have been extensively performed by using a 3D Panel Method code developed by CIRA, namely SIM (Surface Impact Method) [5]. This tool at high supersonic and hypersonic speeds is able to accomplish the preliminary aerodynamic and aerothermodynamic analyses of a complex re-entry vehicle configuration by using simplified approaches as local surface inclination and approximate boundary-layer methods, thus avoiding the time consuming and complex grid generation and computation processes of CFD. The vehicle surface is approximated by a system of planar panels; the lowest level of geometry used in the analysis is a quadrilateral element (see Fig.17). The pressure acting on each panel is evaluated by user-specified compression-expansion and approximate boundary-layer methods.

3.2 CFD-based tool

Numerical tool used to carry out the CFD analyses is the CIRA code H3NS [6]. It solves the flowfield governing equations, including chemical and vibrational non-equilibrium, with a finite volume approach. The fluid is treated as a mixture of perfect gases and the energy exchange between vibrational and translational modes (TV) is modelled with the classical Landau-Teller non-equilibrium equation, with average relaxation times taken from the Millikan-White theory modified by Park. For what concerns transport coefficients, the viscosity of the single species is evaluated by a fit of collision integrals calculated by Yun and Mason, the thermal conductivity is calculated by means of the Eucken law; the viscosity and thermal conductivity of the gas mixture are then calculated by using the semi-empirical Wilke formulas. The diffusion of the multi-component gas is computed through a sum rule of the binary diffusivities of each couple of species (from the tabulated collision integrals of Yun and Mason). Transport coefficients, in the hypothesis of an ideal gas, are derived from Sutherland law, suitably modified to take into account low temperature conditions. With respect to the numerical formulation, conservation equations, in integral form, are discretized with a finite volume, cell centered technique. Eulerian fluxes are computed with a flux difference splitting upwind scheme. Second

order formulation is obtained by means of an ENO-like reconstruction of cell interface values. Viscous flux is computed with a classical centred scheme i.e. computing the gradients of flow variables at cell interfaces by means of Gauss theorem. Integration in time is performed by employing an explicit multistage Runge-Kutta algorithm coupled with an implicit evaluation of the species and vibration energies source terms. Also a parallel version of the code is currently available.

3.3 Flow Radiation assessment tool

The flow radiative heat flux at the SRV wall has been computed through the code PARADE, starting from the results of the fluid dynamic computations (in terms of gas composition and temperature)[4]. This code is able to compute flow-field emission and absorption, between the shock layer and the surface of the probe. The spectral emission and absorption are determined as function of transition level (from upper level to lower level) and emitting population of this level. The population can be derived from the Quasi-Steady-State (QSS) method or by a Boltzmann method in order to take into account the non-equilibrium or equilibrium regime respectively. The radiative computations have been performed with the Boltzmann assumption for the determination of the population of the excited molecular states.

The radiative heat transfer equation (RTE) has been then solved using the one dimensional tangent slab approximation (radiation properties are assumed to vary only in the direction normal to the wall). The intensity of radiation at a given wavelength λ satisfied the equation of radiative transfer:

$$\frac{\partial I_\lambda}{\partial s} = j_\lambda - k_\lambda I_\lambda \qquad (1)$$

where j_λ and k_λ are respectively the emission and absorption coefficients, computed through PARADE. These coefficients are integrated along straight lines toward the wall according to the above equation to computed I_λ. Radiative heat flux at a given wavelength λ is then obtained through integration of I_λ over the solid angle whereas the total radiative heat flux is obtained through integration over the spectrum of interest. In particular, a spectral region between 100 and 40000 nm using 50000 spectral grid locations has been considered in the calculations.

4 Numerical Results

CFD simulations are performed at several discrete points within the SRV flight scenario (i.e., trajectory-based approach), and the results are used to address vehicle AEDB and ATDB. In particular, fifteen trajectory points (TP) have been considered to perform 18 NS 2D axy-symmetric non-equilibrium CFD simulations. Those points are shown in Fig. 4 and has been verified that they lie within the continuum flow regime.

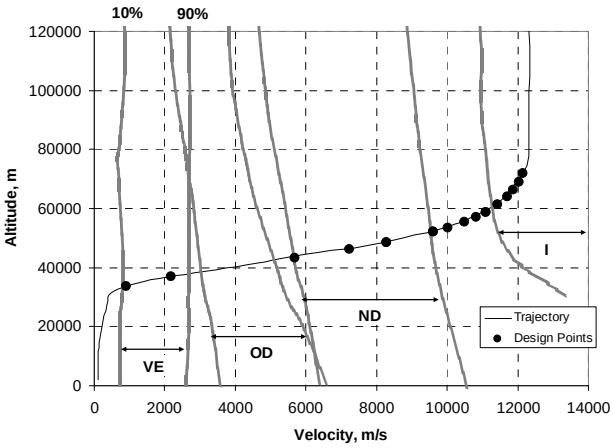

Fig. 4 Reference re-entry trajectory with CFD design points

Further, to take an idea of real gas effects that the capsule will experience during descent, Fig. 4 also shows the reentry trajectory superimposed on the fields (from 10% to 90 %) of vibrational excitation, dissociation, and ionization of flow species [8].

Freestream conditions of design points are summarized in Table 1.

The gas model to consider is air in thermo-chemical non-equilibrium conditions. The model proposed for the air mixture is

constituted by 13 species: N_2, O_2, NO, N, O, Ar, N_2^+, O_2^+, NO^+, N^+, O^+, Ar^+ and e^-.

Design Points Id	Altitude [km]	Velocity [m/s]	Pressure [pa]	Density [kg/m^3]	Temperature [K]	Mach [-]
R1	71.86	12138	4.14	6.78×10^{-5}	212.41	41.54
R7	69.03	12032	6.386	9.95×10^{-5}	223.48	40.14
R8	66.25	11880	9.589	1.42×10^{-4}	234.37	38.70
R2	63.98	11711	13.19	1.88×10^{-4}	243.29	37.45
R9	61.31	11445	18.889	2.59×10^{-4}	253.19	35.87
M1/R3	58.73	11099	26.49	3.57×10^{-4}	258.26	34.45
R10	57.07	10816	32.835	4.37×10^{-4}	261.52	33.07
R4	55.46	10490	40.33	5.30×10^{-4}	264.69	32.16
R11	53.53	10022	51.459	6.67×10^{-4}	268.49	30.50
M2/R5	52.05	9604	61.84	7.95×10^{-4}	270.65	29.12
M3/R6	48.36	8280	97.84	1.25×10^{-3}	270.65	25.11
R12	46.04	7230	130.72	1.70×10^{-3}	267.03	22.07
M4	43.14	5681	189.53	2.54×10^{-3}	259.02	17.61
M5	36.93	2181	437.43	6.30×10^{-3}	241.86	7.00
M6	33.62	922	701.11	1.04×10^{-2}	232.69	3.02

Table 1: Freestream conditions of design points.

Chemical kinetics and reaction mechanism (i.e., 13 species and 22 chemical reactions with third body efficiency) are due to Park [9].

Further, a two temperatures model for thermal non-equilibrium model (e.g., T and T_{vib}) has been considered. Vibrational relaxation is modelled using a Landau-Teller formulation, where relaxation times are obtained from Millikan-White with the high temperature correction Park [8]. Finally, CFD computations are in turbulent flow conditions for points below 52 km altitude.

4.1 Computational Domains, Boundary conditions and solutions convergence

CFD computations have been carried out on multiblock structured grids generated with the commercial tool ICEM-CFD. Two kinds of computational domain, similar to those shown in Fig. 5, have been considered.

The effective dimensions of the outflow boundary, axis and outer boundary are modified in each simulation in order to obtain a grid compliant with the flowfield conditions to simulate.

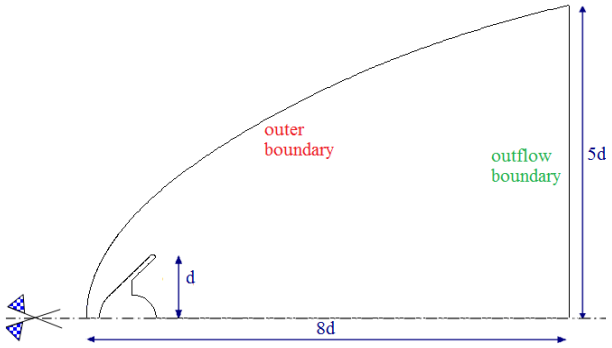

(a - *whole domain*)

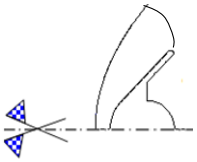

(b - *front shield only*)

Fig. 5 Computational domains. Whole domain (a) and front shield only (b).

Close-up views of 2-D axis-symmetric mesh for both whole and front shield domains can be seen in Fig. 6.

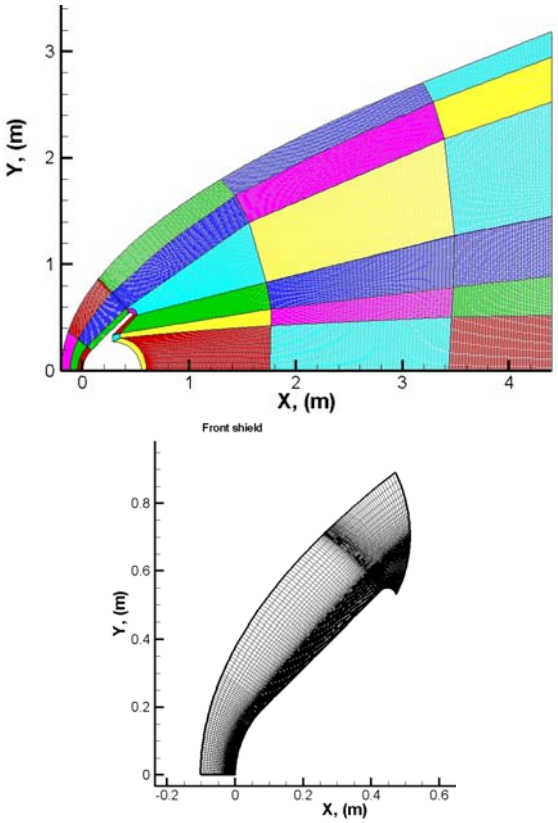

Fig. 6 CFD multiblock for whole domain and front shield case.

The generic whole domain grid has consisted of about 30 blocks for an overall number of about 72000 cells; while in the case of front shield there are 9 blocks for an overall number of about 20000 cells. The minimum spacing at the wall is equal to 10^{-6} m to accurately predict heat transfer at the vehicle surface. When the flow is in turbulent conditions grids use y^+ less than 1; y^+ is defined as:

$$y^+ = \frac{\eta\rho}{\mu}\sqrt{\frac{\tau_w}{\rho}} \qquad (2)$$

where the quantities η and τ_w are the surface normal distance and the shear stress, respectively.

As far as boundary conditions are concerned all CFD computations have been carried out with the assumption of Fully catalytic wall (FCW) at 1000 K temperature.

All CFD results refer to both converged and grid independent computations. Mesh sensitivity analyses have been carried out on three levels of the structured multi-block grid (L_1, L_2, L_3) and the Richardson extrapolation criteria has been applied [11]. The medium grid (L_2) is obtained by halving the size of cells of the coarse (L_1) grid. Similarly, the finer grid (L_3) is obtained halving the size of cells of the medium grid.

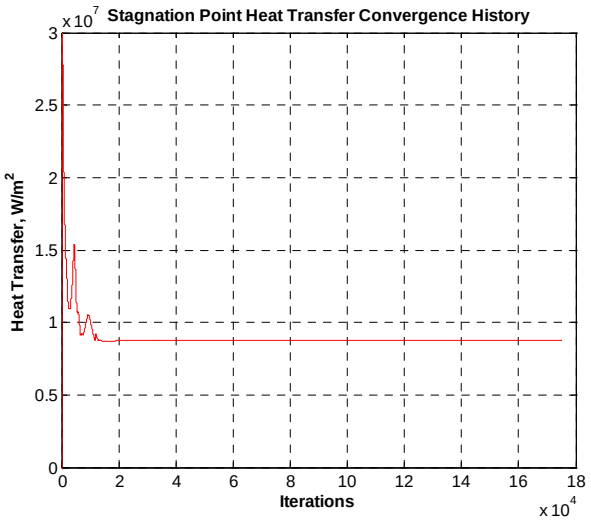

Fig. 7 Stagnation point heat flux vs. iterations for M1 simulation.

In order to assess numerical solution convergence, equation residuals and aerodynamic coefficient (i.e. C_D) as well as the stagnation point heat flux have been monitored during iterations. Solution convergence is assumed when equation residuals drop more than three orders of magnitude and both the aerodynamic coefficient and the stagnation point heat flux plots are flat for enough iterations. For example, Fig. 7 shows the stagnation point heat flux convergence histories for the M1 simulation.

4.2 Flowfield Analysis

In the hypersonic portion of the re-entry, the flow is dominated by a strong bow shock and is characterized by a thin shock layer and more other characteristics flowfield features as those described in Fig. 9. This figure has been reported, as a reference, to understand flowfield results hereinafter discussed. [12].

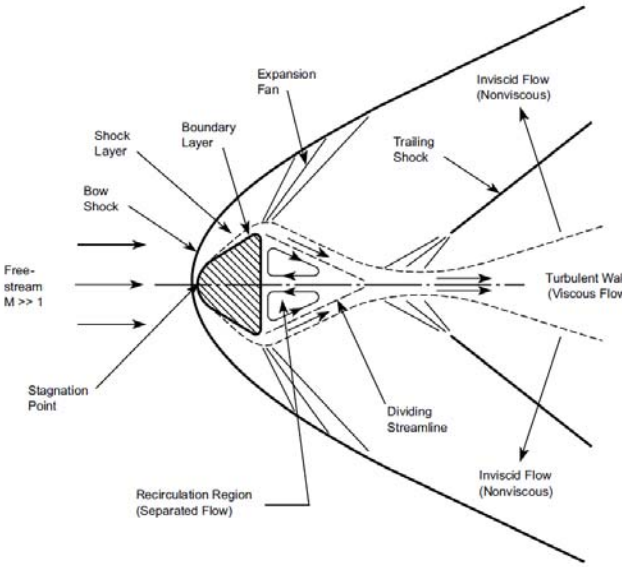

Fig. 8 Characteristics of hypersonic flow around a blunt body (right side) [12].

The pressure and Mach number contours for M_∞=3.02 (i.e., M6 TP) are shown in Fig. 9. As shown, the bow shock is well resolved by the adopted spatial discretization. This shock wave causes a large sonic region, a smooth conical flow along the SRV conical part, and a strong flow expansion at the shoulder. The cone angle after the rounded stagnation region causes

the curvature of the shock wave therefore to the presence of an entropy layer that affects the results at the wall.

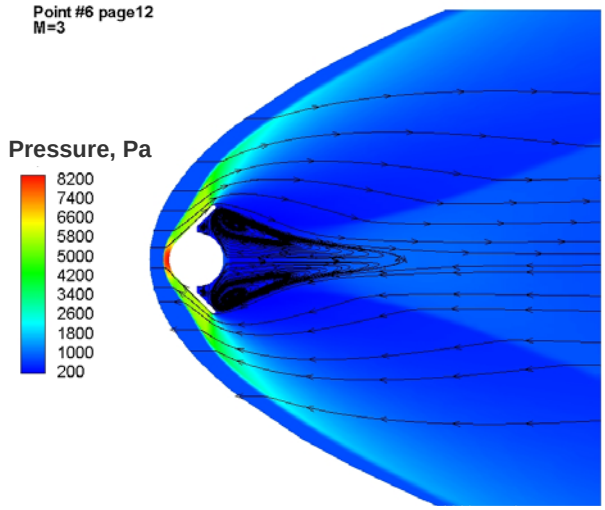

Fig. 9 Static Pressure at M6 TP.

Streamlines are also shown in Fig. 9 in order to appreciate the flowfield structure surrounding the vehicle, especially the complexity of the wake flow. A strong base expansion together with a vortex feature can be appreciated as well. In particular, at the rearward facing base of the body the flow separates and creates a region of recirculating flow bounded by dividing streamlines.

The Mach number and the static temperature fields past the SRV at M4 TP are shown in Fig.10 and Fig. 12, respectively.

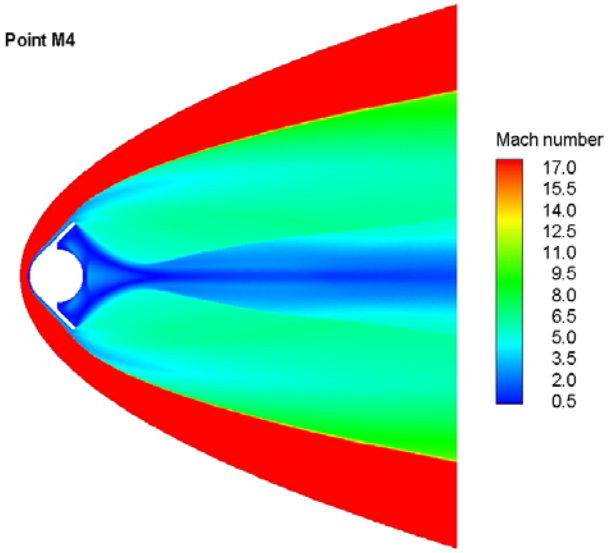

Fig. 10 Mach number contours at M4 TP.

Fig. 11 highlights that as the air crosses the strong bow shock it is suddenly heated thus reaching a temperature of the order of 8000 K. It also shows that the shear layer, starting from the SRV shoulder, converges on the capsule axis, undergoing normal shock at the neck of this flow, from which develops an oblique trailing shock wave, ultimately forming a viscous core or inner wake. Fluid in the inviscid wake crosses the trailing shock, increasing pressure, temperature, and density thereby, and in continuing downstream this outer wake merges with the inner wake. Illustrated in Fig. 11 is also the presence of a rapid expansion as the highly compressed gas flows around the shoulder of the capsule.

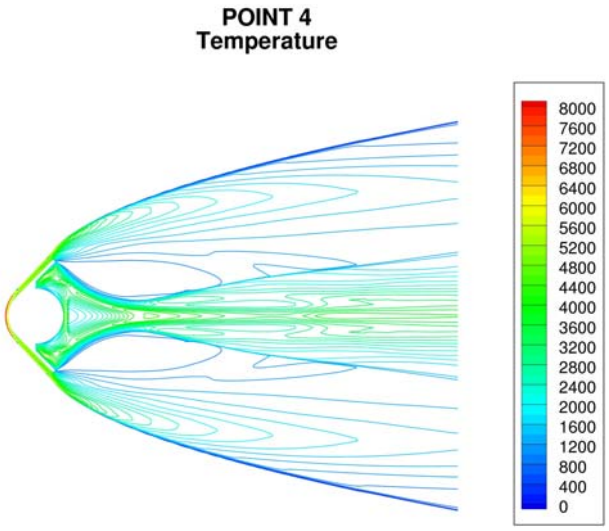

Fig. 11 Temperature contours at M4 TP.

This expansion, dominated by inviscid effects, has the effect of rapidly lowering the translational temperature, density and pressure of the gas, while the chemical state of the gas and the temperatures, that characterize the energy in the internal modes, tend to remain frozen and the gas is still dissociated and excited.

Fig. 12 and Fig. 13 show the static pressure and Mach number fields characterising the shock layer at M1 flight conditions. As shown, a very strong shock wave is generated in front of the capsule due to the very high Mach number (i.e., M_∞=34.45). Indeed, as the capsule enters into the Earth's atmosphere directly from the hyperbolic Earth-return trajectory, the

atmospheric entry speed of SRV is over 12 km/s (see Fig. 4).

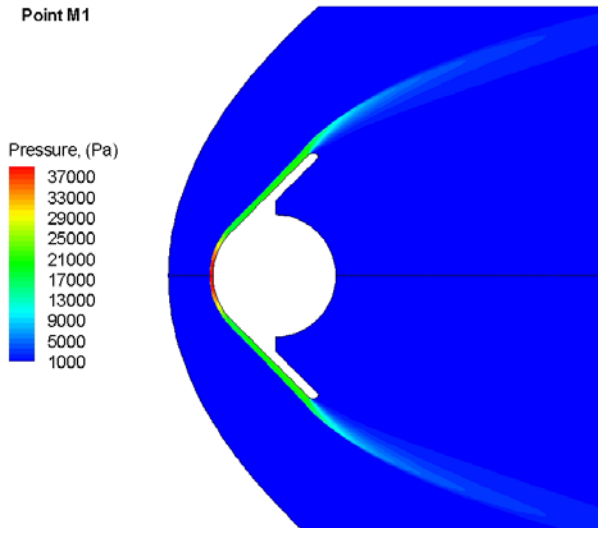

Fig. 12 Pressure contours at M1 TP.

Therefore, the shock layer gas is much more highly heated that the case of a normal Earth orbital re-entry. As a consequence, a large contribution to the vehicle aeroheating comes by the radiative heating of the plasma flow within the shock layer. This must be taken into account for the SRV TPS design.

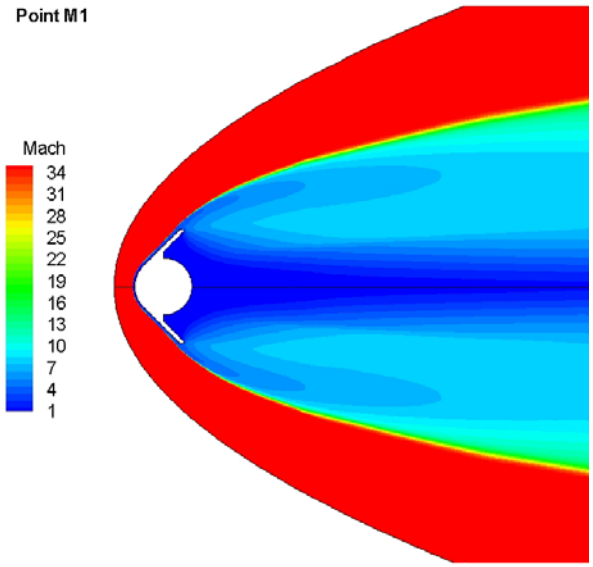

Fig. 13 Mach number contours at M1 TP.

Such a strong shock wave causes molecules of atmosphere to be dissociated and ionized, and consequently the shock layer gas consists of molecules, atoms, ions and electrons. Static temperature distribution along with the capsule's stagnation line is given in Fig. 14, in which translational and vibrational temperatures distributions are also highlighted.

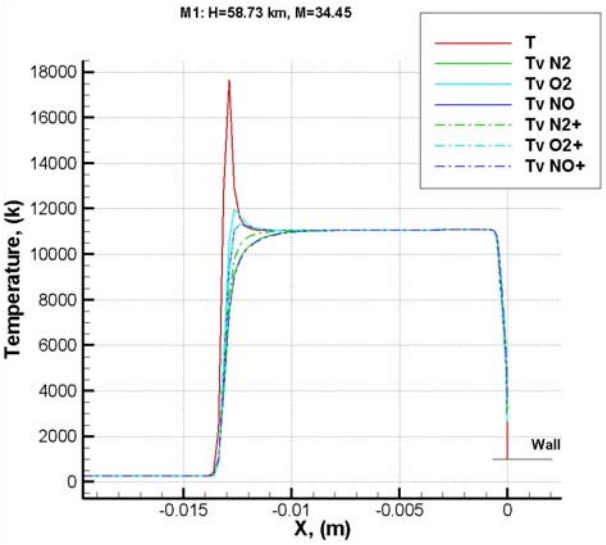

Fig. 14 Temperatures along with the stagnation line at M1 TP.

As one can see, the temperature behind the bow shock wave is very high thus causing the complete Oxygen and Nitrogen dissociation inside the shock layer, as clearly illustrated in Fig. 15.

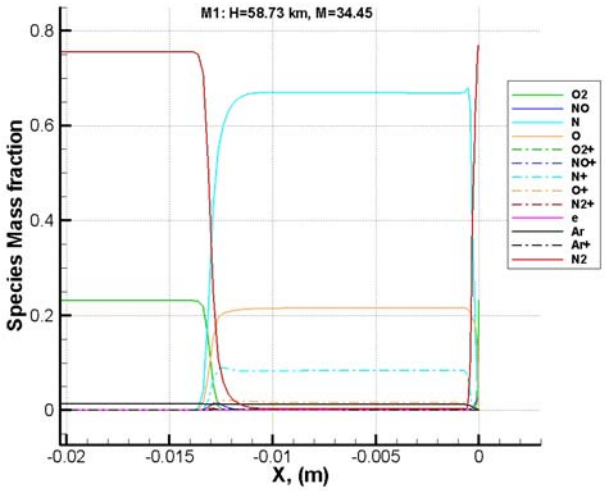

Fig. 15 Species mass fraction along with the stagnation line at M1 TP.

In particular, this figure together with Fig.14, show also that a large portion of the shock layer is in thermo-chemical equilibrium (i.e., the temperature profiles are quite flat until

the boundary layer is reached) and only near the shock and in the boundary layer there is a departure from this state: the non-equilibrium region is just downstream the bow shock wave, and the size is of the order of the shock wave thickness.

Moreover, the temperature trends exhibit a sharp discontinuity at the shock wave with a rapid decreasing behind the bow shock due to finite rate dissociation of molecules. For instance, the translational-rotational temperature, T, reaches the maximum value at about x=14 mm, while the vibrational-electronic temperature, T_v, is still much lower than T. T_v begins to be equilibrated around x=10 mm and continues to be equilibrated until the surface.

On the contrary, the thermal non-equilibrium is observed at the region adjacent to the equilibrium one; i.e., from x=14 mm to 10 mm. The equilibrated temperature amounts up to about 11000 K.

Fig. 15 also explains the distribution of the mass fraction of the neutral, and ionized species along with the stagnation line. As shown, N_2 and O_2 molecules dissociate rapidly and, successively, the generation of NO molecule, the atomic nitrogen and oxygen, and the ionization of the molecules such as N_2, O_2 and NO, occur rapidly in the thermal non-equilibrium region. In general the level of each formed species reaches a state of near chemical equilibrium for a large portion of the shock layer. Then, at the edge of the boundary layer the levels of the species start to change rapidly again as the temperature falls and density rises through the boundary layer: N and O recombine to their molecular forms resulting in an increase in the levels of N_2 and O_2 and a fall in the levels of N and O. The reason for this is that the ionised species recombine with the electrons to form neutral species of N, O, N_2 and O_2, and NO.

Concerning the ionic species, there are substantial levels of O^+ and N^+ while very low mass fractions of N_2^+, O_2^+ and NO^+. In fact, crossing the shock O_2 is rapidly and highly dissociated to form O and O^+. N_2 is dissociated to form N and NO by recombination with O but a small fraction of NO is created. A large part of the atomic nitrogen produced by the dissociation of N_2 is ionized in N^+. Note that the ionization process is very important considering that it has a non negligible impact on radiative heat flux at high velocity flight conditions.

Finally, heat fluxes distribution at wall for M1, M2, and M3 CFD computations is shown in Fig. 16.

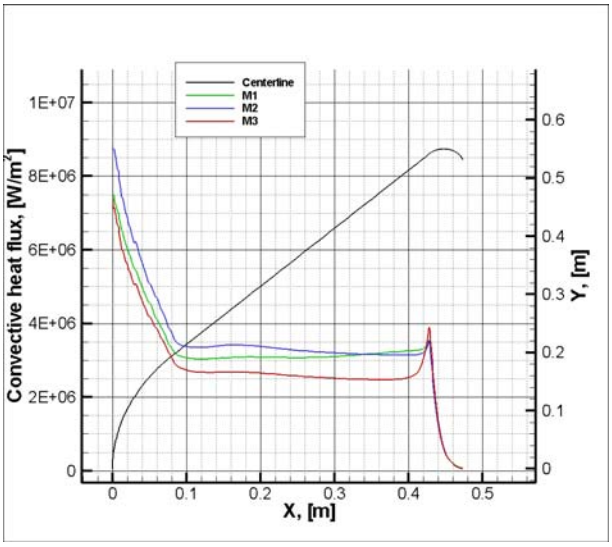

Fig. 16 Convective heat flux for M1, M2, and M3 TP

As shown, the trajectory point M2, i.e. the point characterized by the maximum aeroheating, the heat flux is equal to about 8750 kW/m^2 at the stagnation point and 3500 kW/m^2 at the capsule shoulder, where the boundary layer thickness decreases for the effect of the strong expansion.

With the density, the molar fractions and the two temperatures (translational and vibrational one) field evaluated by CFD simulations of all the R trajectory points, the radiation heat flux has been computed with PARADE [4]. Results, in terms of radiative and convective heat fluxes at the wall, are shown in Fig. 17.

As shown, the radiative heat flux is greater at the stagnation point, reaching a value of about 6000 kW/m^2 at the R3 TP, and then it decreases along with the front shield. Therefore, this additional contribution of surface heating must be taken into account in designing the SRV thermal protection system. In particular, after the peak heating at the stagnation point, the

convective heat flux decreases along with the surface as the boundary layer develops up to an inflection point that corresponds at the end of the spherical shape of the capsule.

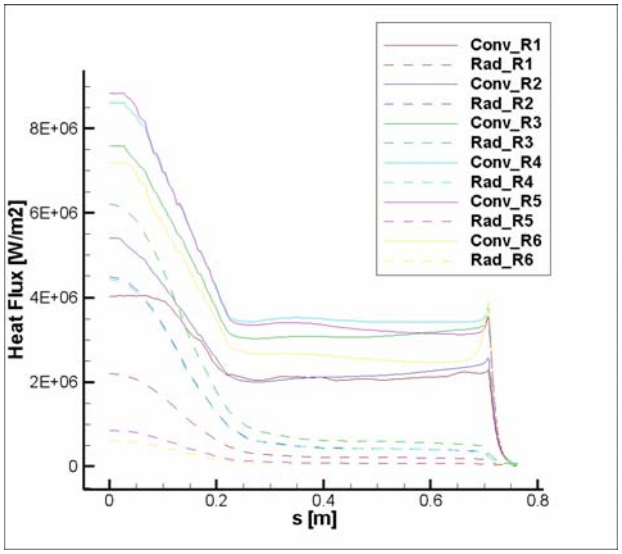

Fig. 17 Convective and radiative heat fluxes comparison for R1-R6 TPs.

Along the conical part it continues to decrease with a different shape and then it increases near the shoulder due to the small radius of curvature and the expansion that causes a reduction of the boundary layer thickness.

Radiative heat flux profiles for the remaining R7 to R12 cases are quite the same as those of R1 to R6 reported in Fig. 17 and, therefore, are left for brevity.

Finally, it is worth to note that no full coupled computations were undertaken since they represent a very prohibitive computational effort.

4.3 SRV Aerodynamics

SRV aerodynamics is shown in term of lift (C_L), drag (C_D), and pitching moment (C_M) coefficients (only drag in CFD analysis).

$$C_L = \frac{L}{\frac{1}{2}\rho_\infty v_\infty^2 S_{ref}} \qquad (3)$$

$$C_D = \frac{D}{\frac{1}{2}\rho_\infty v_\infty^2 S_{ref}} \qquad (4)$$

$$C_M = \frac{M_y}{\frac{1}{2}\rho_\infty v_\infty^2 L_{ref} S_{ref}} \qquad (5)$$

The geometric reference parameters that have been chosen in order to make aerodynamic forces non-dimensional coefficients are S_{ref} =0.95 m^2 (i.e., maximum SRV cross section area) and L_{ref} =1.1 m (i.e., maximum SRV diameter).

Fig. 18 shows a typical mesh surface of SRV that has been used for the engineering-level computations.

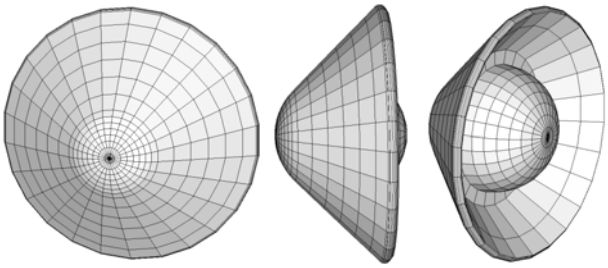

Fig. 18 SRV panel mesh

As an example of engineering level results, the static pressure distributions over the wetted vehicle surface for M_∞=25 and for two angles of attack: 0 and 10 deg are summarized in **Fig. 19** and Fig. 20, respectively.

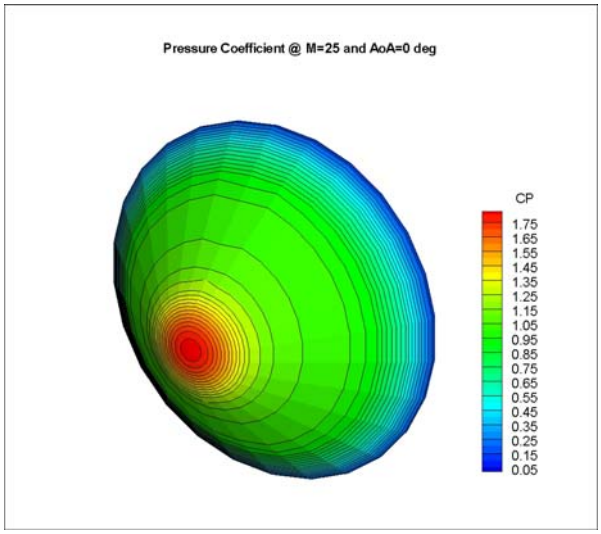

Fig. 19 Cp at M_∞=25 and AoA=0 deg

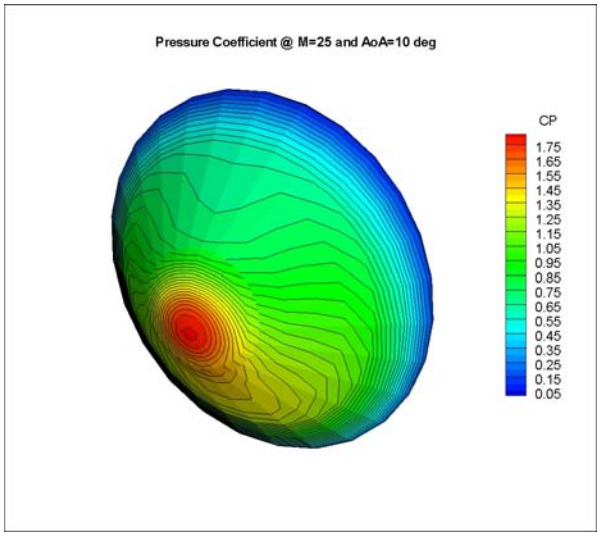

Fig. 20 Cp at M_∞=25 and AoA=10 deg

As shown, when the AoA increases the surface pressure distribution changes thus increasing on the capsule windside, as expected. At the same time flow expansion on the capsule leeside determines locally lower pressure contours.

The lift and drag coefficients for AoA ranging from 0 to 180 deg, in hypersonic conditions, are summarized in Fig. 21.

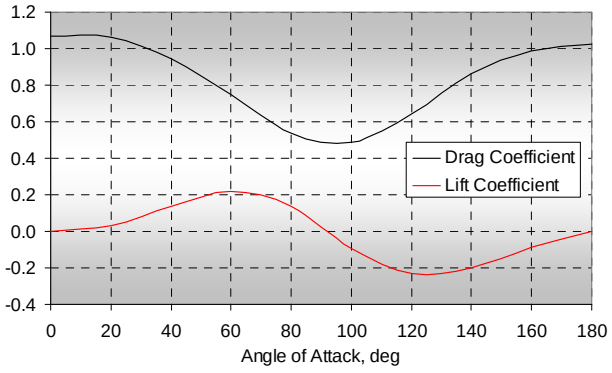

Fig. 21 Lift and Drag coefficients of SRV in hypersonic regime

Results provided for aerodynamic drag agree with analytical results available for blunt cone at hypersonic speed. Indeed, for a blunt cone with a semivertex angle θ_c, nose radius R_N, and base radius R_B, the drag coefficient reads [12]:

$$C_D = 2\sin^2\theta_c + \left(\frac{R_N}{R_B}\right)^2 \cos^4\theta_c \qquad (6)$$

C_D is shown as a function of bluntness ratio R_N/R_B and cone-section semivertex angle θ_C in Fig. 22.

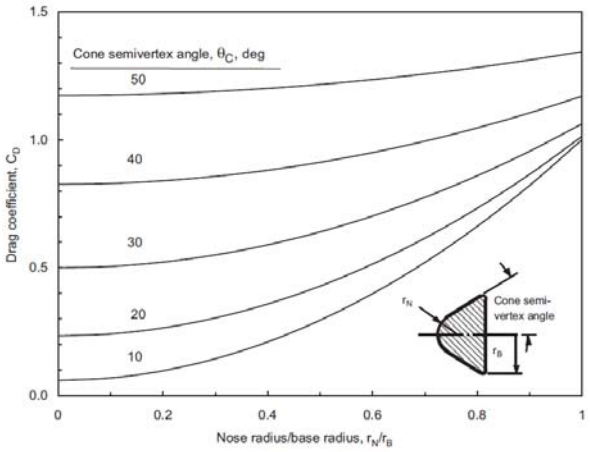

Fig. 22 Hypersonic drag coefficient for sphere-cones [10][12]

In the present case the nose to base radius ratio is equal to 0.5. Therefore, analytical and engineering-based results compare quite good each other. Moreover, preliminary aerodynamic computations in hypersonic regime have been carried out to study also aerodynamic backward static stability of the probe during re-entry trajectory with a center-of-gravity located at 26.5 % of diameter. Indeed, Fig. 23 shows the pitching moment coefficient of SRV in hypersonic regime for AoA varying from 0 to 180 deg.

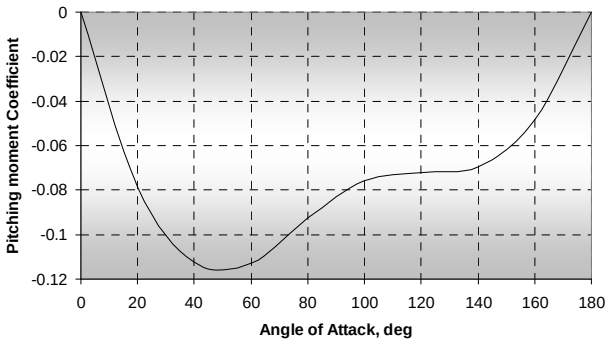

Fig. 23 Pitching moment coefficient of SRV in hypersonic regime

As illustrated in Fig. 23, the chosen aeroshape has two trim angles-of-attack where the pitching moment at the center of gravity is equal to zero (Cm=0 at AoA=0 and 180 deg).

But, for the 180 deg AoA, the slope of the pitching coefficient (Cm_α) is positive and consequently the aeroshape has only one single stable position for AoA=0 deg. This ensures that the probe will not perform a backward re-entry in hypersonic regime.

Capsule drag coefficients have been also evaluated in all performed CFD computations.

Comparison among present CFD results and literature data is shown in Fig. 24 [1].

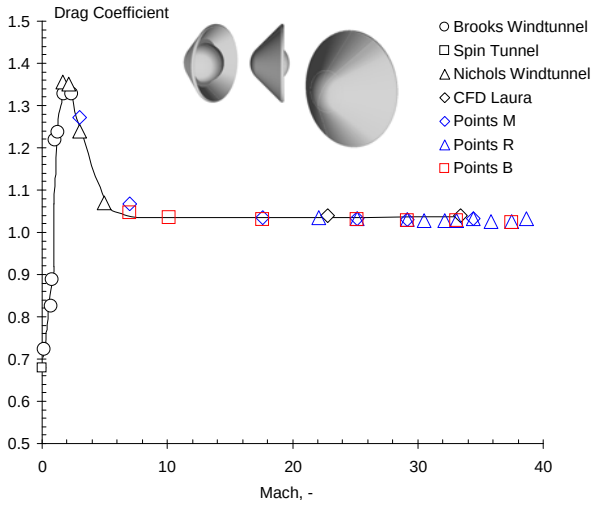

Fig. 24 Drag coefficient of SRV comparison among present and literature results [1]

This diagram presents an approximation of the drag coefficient across the whole Mach range for the SRV. The hypersonic value, 1.07, was computed at Mach 31.8 and 21.5 using the Langley Aerothermodynamic Upwind Relaxation Algorithm (LAURA) [1]. The subsonic value, 0.65, comes from tests conducted in the Langely 20-foot Vertical Spin Tunnel. The supersonic and transonic values are from Brooks and Nichols wind tunnel data on a similar geometry. For the purposes of this feasibility study, the important values are the hypersonic value, which affects the heat pulse, and the subsonic value that determines the impact velocity [1].

As one can see, drag coefficients of the present evaluation compare rather well with literature data, especially at very high Mach number flow conditions. Below Mach 7, however, some differences are recognized due to the effect of base drag.

Difference in the back shell configuration between SRV and the capsule considered in the literature are reported in Fig. 25.

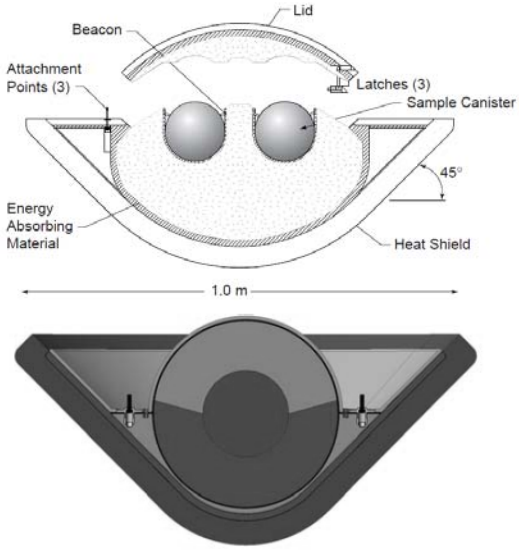

Fig. 25 SRV configuration comparison [1]

5 Conclusions

In this work, numerical simulations have been undertaken for a super-orbital re-entry capsule. A design analysis was performed to determine the aerothermal (i.e., both aerodynamic and aerothermodynamic) performances of an entirely passive Earth entry capsule for Sample Return mission. In particular, this work is useful to assess the aerodynamic performances and stability along with the entry trajectory path.

Present design result refers to both numerical and engineering-based analysis of a 1.1 m diameter spherically-blunted 45-deg half-angle forebody with a low-density, ablative heatshield.

Engineering-based design has been applied to assess flow field regime and capsule aerodynamics; while Navier-Stokes simulations have been conducted to evaluate flow field past the capsule to perform radiation analysis by means of PARADE code. Results of the analysis are presented and discussed.

References

[1] A passive Earth-Entry Capsule for Mars Sample Return. 51st International Astronautics Federation Congress, Rio de Janeiro. 1998. IAF-00-Q.3.04.

[2] Scott, C. D., Ried, R. C., Maraia, R. J., Li, C. P., and Derry, S. M., "An AOTV Aeroheating and Thermal Protection Study," H. F. Nelson (ed.), Thermal Design of Aeroassisted Orbital Transfer Vehicles, Vol. 96 of Progress in Astronautics and Aeronautics, AIAA,New York, 1985, pp. 198-229.

[3] Tauber M. E. and Suttont, K. "Stagnation-Point Radiative Heating Relations for Earth and Mars Entries". Journal of Spacecraft and Rockets. VOL. 28, NO. 1 (pag.40-42).

[4] PLASMA RADIATION DATABASE PARADE V2.2. Report TR28/96

[5] USV_X-Phase A Aerodynamic and Aerothermodynamic Analysis. Report CIRA-CF-06-1393.

[6] CLAE Project. H3NS: Code Development Verification and Validation. Report CIRA-CF-06-1017

[7] BLAST Project: Input to ENG033 – Aerothermodynamic Database. Report CIRA-CF-09-1271

[8] Anderson, Hypersonic and High Temperature Gas Dynamics. McGraw-Hill Book Company, New York 1989

[9] Review of Chemical Kinetic Problems of Future NASA Missions: Earth Entries. Journal of Thermophysics and Heat Transfer Vol 7. No 3. 1993.

[10] Bertin, Hypersonic Aerothermodynamics. AIAA Educational Series, Washington. 1994

[11] Verification and Validation in Computational Science and Engineering. Hermosa Publishers, Socorro, New Mexico. 1998

[12] Notes on Earth Atmospheric Entry for Mars Sample Return Missions. NASA/TP–2006-213486. 2006

Copyright Statement